Materials Science & Engineering A 792 (2020) 139785

Contents lists available at ScienceDirect

Materials Science & Engineering A

journal homepage: http://www.elsevier.com/locate/msea

# On the hydrogen embrittlement behavior of nickel-based alloys: Alloys 718 and 725

Xu Lu[a,*], Yan Ma[b,c], Dong Wang[a]

[a] Department of Mechanical and Industrial Engineering, Norwegian University of Science and Technology, Richard Birkelands vei 2B, No-7491, Trondheim, Norway
[b] Steel Institute (IEHK), RWTH Aachen University, Intzestraße 1, D-52072, Aachen, Germany
[c] Max-Plank-Institut für Eisenforschung GmbH, Max-Planck-Straße 1, D-40237, Düsseldorf, Germany

## ARTICLE INFO

*Keywords:*
Hydrogen embrittlement
Nickel-based superalloys
Intergranular precipitates
Grain boundary
Hydrogen-induced cracking

## ABSTRACT

Nickel-based superalloys have attracted immense attention in the oil and gas industry due to their outstanding combination of mechanical properties and corrosion resistance. In corrosive service environment, hydrogen embrittlement is a severe issue. In the present work, the susceptibility of two precipitation-hardened nickel-based alloys, *i.e.*, Alloy 718 and Alloy 725, to hydrogen embrittlement was studied using slow strain-rate tensile test and advanced characterization techniques. The mechanical properties and fracture behavior of these two alloys were compared in both hydrogen-free and hydrogen-charged conditions. In the presence of hydrogen, Alloy 718 failed prevalently through a combination of transgranular and intergranular cracking behavior, while Alloy 725 failed primarily through intergranular failure with a considerably lower resistance to hydrogen embrittlement. This distinction was attributed to their different microstructures and different types of precipitates along grain boundaries. Specifically, in Alloy 725, the decoration of (Cr, Mo)-rich precipitates at grain boundaries distort the local structures and cause such boundaries to be vulnerable to hydrogen attack, thus promoting intergranular cracking.

## 1. Introduction

Materials used in the oil and gas industry always encounter challenges from high-pressure-high-temperature environments and attacks from corrosive gases containing large amounts of $CO_2$ and $H_2S$. Such service conditions require structural materials to possess both high strength and good corrosion resistance. Satisfying these demands, nickel (Ni)-based superalloys have attracted immense attention in the oil and gas industry since they were used for downhole equipment in the early 1980s [1]. In particular, precipitation-hardened Ni-based superalloys (*e.g.* commercial Alloy 718 and Alloy 725) are widely used in oilfield and subsea constructions owing to their good mechanical properties over a broad range of temperatures. In such alloys, the elements Mo and Cr are responsible for the superior corrosion resistance. However, Alloy 718 is usually susceptible to localized corrosion when sulfur and halide ions are present, because of its intermediate Cr (~17–21 wt%) and Mo (~2.8–3.3 wt%) content [1–3]. Thus, by further increasing the content of Mo up to ~7.0–9.5 wt%, Alloy 725 has been introduced for severely corrosive applications with improved resistance to, particularly, pitting and crevice corrosion [1]. To ensure high strength, other elements such as Nb, Ti, and Al are alloyed for precipitation hardening. The main strengthening phase is the homogeneously distributed coherent and metastable γ'', which has a body-centered tetragonal $D0_{22}$ structure with a chemical formula of $Ni_3Nb$. Another strengthening phase is the face-centered cubic γ' in a form of spherical or cuboidal $Ni_3(Al, Ti)$ [4]. In addition, the orthorhombic δ phase ($Ni_3Nb$), hexagonal η phase ($Ni_3Ti$), topologically close-packed σ phase (composed of Ni, Cr, Co, Mo, *etc.*) [5] and various carbides and carbonitrides can form along grain boundaries (GBs) or in the matrix, depending on different heat treatments.

Hydrogen embrittlement (HE) is another severe issue when these alloys are applied in a corrosive environment. The introduction of hydrogen during cathodic protection or corrosion process can result in the premature failure of the construction materials and catastrophic disasters [6–11]. Several mechanisms have been proposed to explain the HE, such as hydrogen-enhanced localized plasticity (HELP) [12,13], hydrogen-enhanced decohesion (HEDE) [14–16], hydrogen adsorption-induced dislocation emission (AIDE) [17–20], and hydrogen-enhanced strain-induced vacancy (HESIV) [21]. Nevertheless, none of them can exclusively explain all the hydrogen-assisted cracking

---

[*] Corresponding author.
*E-mail addresses:* xu.lu@ntnu.no, luxu1114@gmail.com (X. Lu).

https://doi.org/10.1016/j.msea.2020.139785
Received 28 March 2020; Received in revised form 15 June 2020; Accepted 16 June 2020

phenomena, which are often synergistic effects of several mechanisms.

For precipitation-hardened Alloy 718, hydrogen-assisted cracking has been frequently reported in both transgranular and intergranular manner [7,8,11,22–25]. The transgranular fracture is supposed to result from the formation and coalescence of nanoscale voids along or at the intersections of dislocation slip bands due to hydrogen-dislocation interactions during uniaxial tensile or fatigue tests [22,26]. In contrast, hydrogen-induced intergranular cracking is often observed at GB triple junctions, high-misorientation GBs, and δ-phase-decorated GBs, as a result of strain and stress localization in the concept of HEDE mechanism [24,25,27]. Moreover, a recent study demonstrated that the δ phase at GBs can absorb a higher amount of hydrogen than carbides or nitrides, which promotes decohesion of the δ phase-matrix interfaces [28]. For precipitation-hardened Alloy 725, its susceptibility to HE has been rarely reported. Two recent studies emphasized the role of coherent twin boundaries [29] and GB characteristics [30] in the HE of Alloy 725. The former study postulated that coherent twin boundaries are susceptible to crack initiation but resistant to crack propagation because of different physical mechanisms governing each process [29]. Furthermore, GBs with low-index planes were demonstrated to possess striking resistance to hydrogen-assisted cracking by deflecting the crack path [30]. However, the impact of GB precipitates on the HE behavior in Alloy 725, which are assumed to play an important role in intergranular cracking, was not investigated in the previous studies.

The present study aims to achieve an in-depth understanding of the hydrogen effect on precipitation-hardened Ni-based alloys 718 and 725. The susceptibility of both alloys to HE was studied using the slow strain-rate tensile test and advanced microstructural characterization techniques. The mechanical properties and fracture behaviors of these two alloys were compared in both hydrogen-free and hydrogen-charged conditions. Furthermore, the fracture and HE behaviors of two alloys were discussed in relation to their different microstructures.

## 2. Materials and experimental methods

The nominal compositions of Alloys 718 and 725 are listed in Table 1. These two alloys were subjected to standard API heat treatments aimed at specific applications. Alloy 718 was received from the supplier, and the as-received alloy was aged at 782 °C for 6.5 h followed by air cooling. A laboratory-melt Alloy 725 was produced by vacuum induction melting and forged to a round bar with a diameter of 130 mm. After solution annealing, Alloy 725 was aged in two steps: 732 °C for 8 h and 621 °C for 8 h followed by air cooling.

The effect of hydrogen on the mechanical properties was evaluated by slow strain-rate tensile tests (SSRTs). The geometry of the two-step dog-bone sample for the SSRTs is shown in Fig. 1. Each alloy was tested under two conditions *i.e.*, hydrogen-free and hydrogen-charged. Before SSRTs and hydrogen pre-charging, the samples were mechanically ground up to 4000 grit and polished with 3- and 1-μm diamond pastes. Electropolishing in a methanolic $H_2SO_4$ solution at 26 V for 30 s was applied as the final step to remove the deformed layer caused by mechanical polishing. Hydrogen pre-charging on the SSRT specimens was performed in a mixture of glycerol and $H_3PO_4$ [31] for 18 h at a cathodic current density of 15 mA/cm$^2$ at 75 °C. This solution guaranteed a corrosion-free surface after electrochemical hydrogen charging [32]. The time between retrieving the sample from the electrolyte and beginning the SSRT was approximately 20 min. The SSRT was conducted at an initial strain rate of $2 \times 10^{-5}$ s$^{-1}$ on a Kammrath & Weiss tensile/compression module in the high vacuum (HV) chamber (4.7E-3 Pa) inside the high-resolution Quanta FEG 650 scanning electron microscope (SEM, Thermo Fisher Scientific Inc., USA).

The microstructure, fractography, surface secondary cracks, and subsurface cracks (on the cross sections) of the alloys after loading to fracture were characterized using backscattered electron (BSE) signal and electron backscatter diffraction (EBSD) technique. The accelerating voltage and the step size for EBSD were 20 kV and 0.8 μm, respectively. For such measurements, the samples were chemomechanically polished using a colloidal silica suspension (Struers OPS) to obtain a high surface quality. The fractured part was electrodeposited with Ni to obtain edge retention during sample preparation to analyze the subsurface damages [33].

The elemental partitioning behavior between the nano-sized precipitates and the matrix was characterized by atom probe tomography (APT). The needle-shaped specimens were prepared using a FEI® Helios™ Nanolab™ 660 focused ion beam (FIB) instrument. APT measurements were performed using a local electrode atom probe (LEAP) 4000X HR instrument operated in laser-pulsing mode with and ultraviolet laser (wavelength 355 nm). The pulse frequency and the laser energy were 250 kHz and 30 pJ, respectively. During the measurements, the base temperature in the analysis chamber was maintained at 60 K. The APT data were reconstructed using the Integrated Visualization and Analysis Software package (IVAS 3.8.0, CAMECA Scientific Instruments, Madison, WI).

To quantify the hydrogen content and investigate the hydrogen trapping behavior, thermal desorption analysis (TDA, G4 Phoenix DH, Bruker Co.) was performed on the hydrogen-charged samples. The dwell time between the TDA test and hydrogen charging was controlled within 20 min, which was identical to the time interval between SSRT and hydrogen charging. The TDA was conducted from 50 to 750 °C at a heating rate of 25 °C/min. The current flow of hydrogen was precisely recorded using a mass spectrometer and presented as a function of temperature or time. The total hydrogen content was obtained by integrating the hydrogen content desorbed from 50 to 750 °C.

## 3. Results

### 3.1. Microstructural analysis of Alloys 718 and 725

Fig. 2 shows the microstructures of precipitation-hardened Alloys 718 and 725, respectively. The average grain size of Alloy 718 was 73.5 μm. Block-shaped carbides and nitrides enriched with Nb and Ti were observed in the matrix (Fig. 2(a)), as illustrated by the energy dispersive spectroscopy (EDS) results (Fig. 2(a3) and (a4)), which were also confirmed in a previous study by the present authors [33]. The majority of GBs in Alloy 718 were not decorated by intergranular precipitates. In some cases, however, δ phase ($Ni_3Nb$) was observed along the GBs (Fig. 2(a1)), as shown by the EDS result in Fig. 2(a5). This type of precipitate was transformed from metastable γ'' during heat treatment [27], resulting in the formation of the associated precipitation free zones adjacent to GBs ((Fig. 2(a1)). The strengthening phases γ' and γ'' were

**Table 1**
Nominal compositions of Alloys 718 and 725 (in wt.%).

| | | | | | | | | |
|---|---|---|---|---|---|---|---|---|
| **Alloy 718** | **Element** | **Ni** | **Fe** | **Cr** | **Nb** | **Mo** | **Ti** | **Al** |
| | **wt. %** | Balance | 19.14 | 17.62 | 4.98 | 2.87 | 0.95 | 0.52 |
| | **Element** | **Co** | **C** | **Si** | **S** | **P** | **B** | **N** |
| | **wt. %** | 0.05 | 0.018 | 0.07 | <0.0003 | 0.008 | 0.004 | trace |
| **Alloy 725** | **Element** | **Ni** | **Fe** | **Cr** | **Nb** | **Mo** | **Ti** | **Al** |
| | **wt. %** | Balance | 10.1 | 19.7 | 3.6 | 7.3 | 1.4 | <0.1 |
| | **Element** | **Mn** | **C** | **Si** | **S** | **P** | **N** | |
| | **wt. %** | <0.02 | <0.01 | <0.1 | <0.001 | <0.005 | trace | |

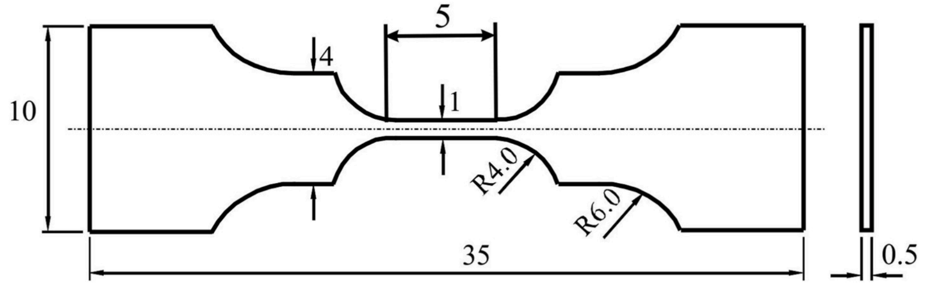

**Fig. 1.** Sample dimensions for the SSRT test (all dimensions are shown in mm).

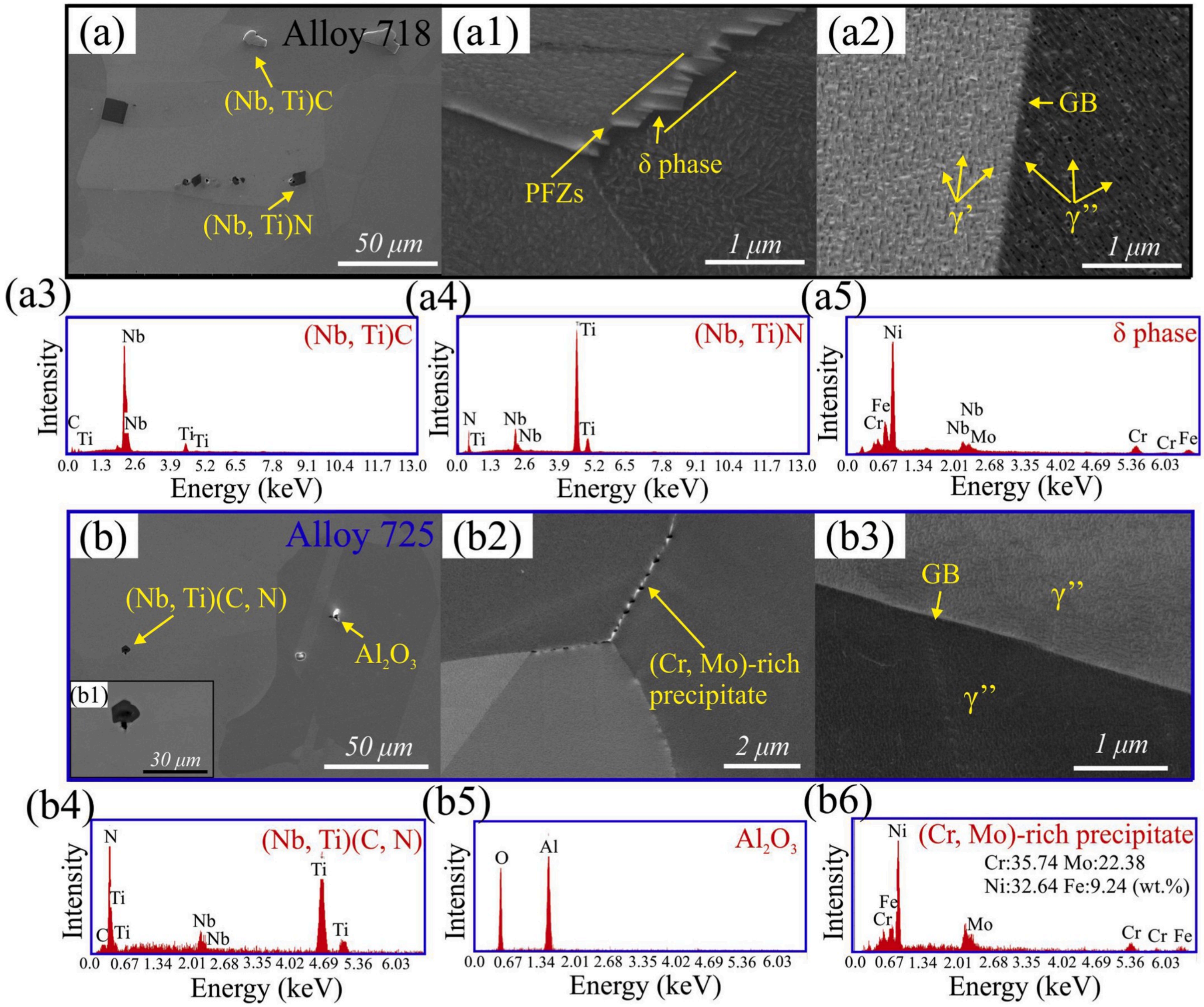

**Fig. 2.** (a) Microstructure of precipitation-hardened Alloy 718 showing (a1) GB precipitates and (a2) γ, γ'' precipitates; (a3)-(a5) EDS analysis of carbide, nitride and δ phase. (b) Microstructure of precipitation-hardened Alloy 725 showing (b1) magnified carbonitride, (b2) GB precipitates and (b3) γ'' precipitates; (b4)-(b6) EDS analysis of carbonitride, $Al_2O_3$ and (Cr, Mo)-rich precipitate. (GB: grain boundary; EDS: energy dispersive spectroscopy; PFZs: precipitation free zones.)

homogeneously distributed in the matrix (Fig. 2(a2)). Fig. 3(a) shows the three-dimensional atom map of the Alloy 718 matrix. It was observed that Ni (~69.85 at.%), Al (~9.24 at.%), Ti (~7.61 at.%), and Nb (~8.71 at.%) were enriched in γ' (Fig. 3(a1)). In comparison, γ'' was strongly enriched in Ni (~68.62 at.%) and Nb (~19.62 at.%) with a small fraction of Ti (~4.11 at.%) (Fig. 3(a2)). Owing to the limited probing volume and the large size of γ'' (~80 nm), the γ'' precipitate was only partially captured (Fig. 3(a)). For Alloy 725, the average grain size was 97.4 μm. In this alloy, carbonitrides (magnified in Fig. 2(b1)) and aluminum oxide ($Al_2O_3$) precipitates were found in the matrix. EDS analysis of these precipitates were shown in Fig. 2(b4)-(b5). It is worth noting that the appearance of $Al_2O_3$ in the matrix emanated from the

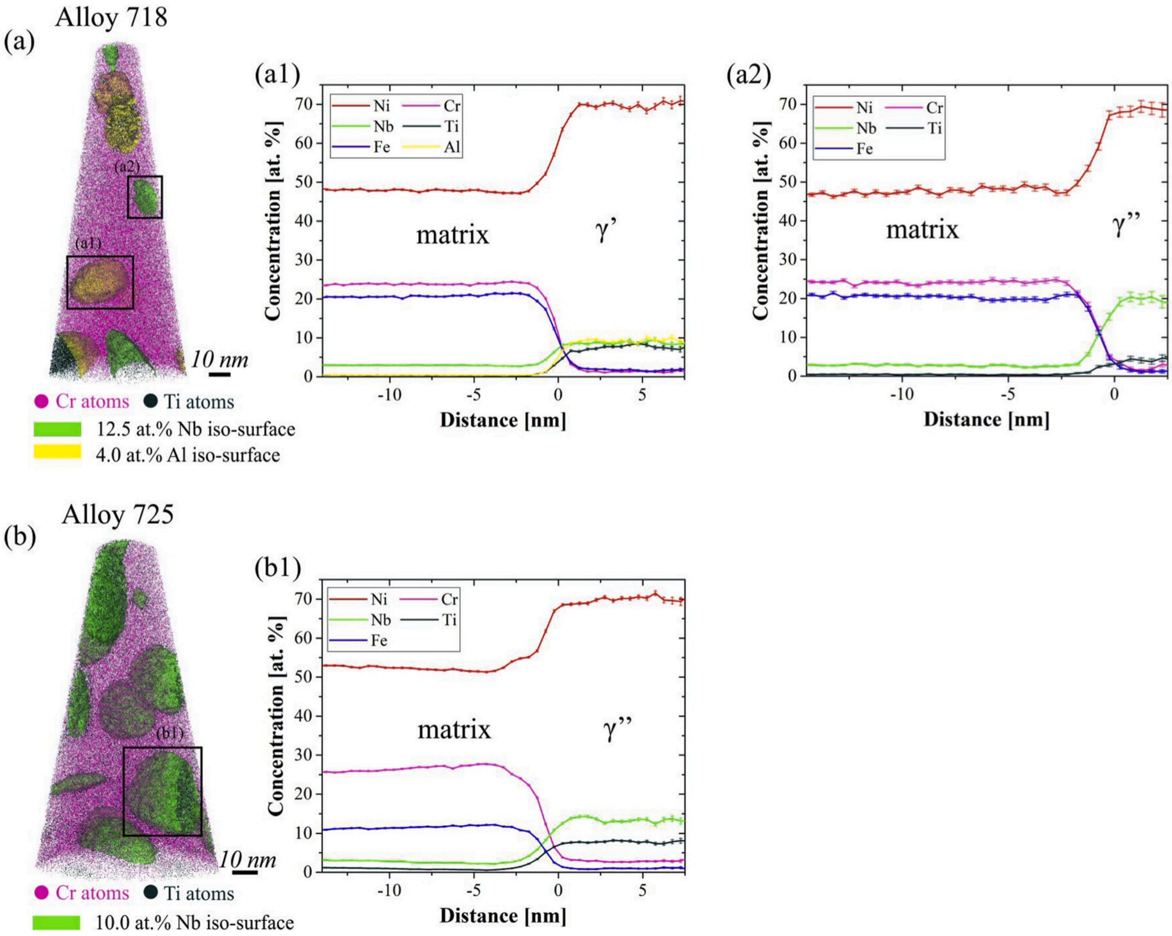

**Fig. 3.** Atom probe tomography analysis: (a) 3D atom map of Alloy 718; 1D concentration profiles of the selected (a1) γ' precipitate and (a2) γ'' precipitate marked in (a). (b) 3D atom map of Alloy 725; (b1) 1D concentration profile of the selected γ'' precipitate marked in (b).

production process due to the remelted process, which is not a typical phase in this alloy. In contrast to Alloy 718, a large volume fraction of GBs in Alloy 725 was decorated by the (Cr, Mo)-rich precipitates (Fig. 2 (b1)) [34]. Element distribution obtained from EDS analysis shows that Cr and Mo partitioned in such precipitates (Fig. 2(b6)). Owing to the existence of precipitates, GBs became irregular and curved (Fig. 4). Only γ'' was detected in Alloy 725 in the APT measurement (Fig. 3(b)). The same as γ'' in Alloy 718, the γ'' precipitates in Alloy 725 were also enriched in Ni (~70.18 at.%), Nb (~13.25 at.%), and a small fraction of Ti (~7.84 at.%). Due to the lower aging temperatures of Alloy 725, the average size (25 nm) and number density ($8.2 \times 10^2$ μm$^{-2}$) of γ'' (Fig. 2 (b3)) were about two times smaller and more than eight times higher than those of γ'' in Alloy 718 (Fig. 2 (a2)). However, the average size of γ' (28 nm) in Alloy 718 was comparable to that of γ'' in Alloy 725.

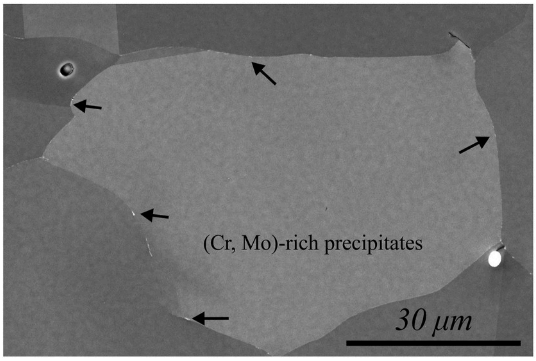

**Fig. 4.** Micrograph of curved grain boundaries due to the decoration of (Cr, Mo)-rich precipitates in Alloy 725.

### 3.2. *Hydrogen trapping behavior*

Fig. 5 shows the hydrogen desorption spectra for both alloys after electrochemical charging. The total detrapped hydrogen content was 27.20 and 25.47 wppm for Alloys 718 and 725, respectively. After deconvolution of the obtained spectra, three desorption peaks were observed for each curve (Fig. 5).

The first peak corresponds to the diffusible hydrogen with a relatively low binding energy to hydrogen, the second peak to the reversibly trapped hydrogen, *i.e.,* hydrogen trapped at γ', γ'', GBs, δ phases, *etc.* [35,36], and the third peak to the irreversibly trapped hydrogen with a high activation energy for detrapping, *i.e.*, hydrogen primarily trapped at carbides [36]. The amount of hydrogen in different trapping sites can be determined by integrating each peak. Given that tested samples have different weights, only the relative hydrogen fraction of each peak was compared to study the hydrogen trapping ability in the two alloys. The relative hydrogen fraction of each peak and the corresponding peak temperature are summarized in Table 2. The results suggested that Alloy 718 contained a comparable amount of diffusible hydrogen, less reversibly trapped hydrogen, and more irreversibly trapped hydrogen than Alloy 725. Moreover, a slight variation was observed in the peak temperatures for both alloys.

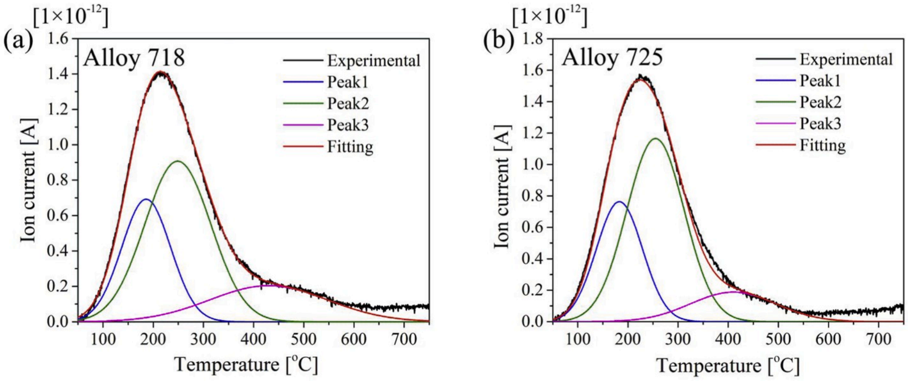

**Fig. 5.** Hydrogen desorption spectra of (a) Alloy 718 and (b) Alloy 725 obtained in thermal desorption analysis experiments including the deconvoluted peaks and the cumulative fitting curve.

**Table 2**
Relative hydrogen fraction and peak temperatures under each trapping condition for Alloys 718 and 725.

| Alloy | Relative hydrogen fraction (%) | | | Peak temperature (°C) | | |
|---|---|---|---|---|---|---|
| | Peak1 | Peak2 | Peak3 | Peak1 | Peak2 | Peak3 |
| Alloy 718 | 28.8 | 50.9 | 20.3 | 186 | 250 | 430 |
| Alloy 725 | 29.7 | 56.8 | 13.5 | 183 | 255 | 410 |

### 3.3. Effect of hydrogen on mechanical properties

Fig. 6 shows the engineering stress-strain curves of both alloys after loading to fracture under hydrogen-free and hydrogen-charged conditions. The strength values for these alloys in this study were slightly lower than the typical values for conventional 718 and 725 alloys used in the oil and gas industries [2]. This discrepancy was due to the sub-sized tensile sample used in this study for the purpose of in-situ observation, instead of a standard sample according to ASTM G129 [37]. In hydrogen-free condition, Alloy 725 exhibited a higher yield strength (YS, defined as 0.2% offset stress; by ~11%), higher ultimate tensile strength (UTS; by ~20%), and slightly lower ductility (total elongation by ~1.7%) than Alloy 718 (Fig. 7(a) and (b)). When hydrogen was introduced, Alloy 718 exhibited a slight increase in YS within the scatter range and a decrease in UTS (by ~10%). Alloy 725 revealed a decrease in both YS (by ~5%) and UTS (by ~31%). Moreover, a dramatic decrease in total elongation by 66.1% and 87.3% was observed for Alloys 718 and 725, respectively (Fig. 7(b)). The engineering stress-strain curve shows that the Alloy 725 failed rapidly after passing the yield point.

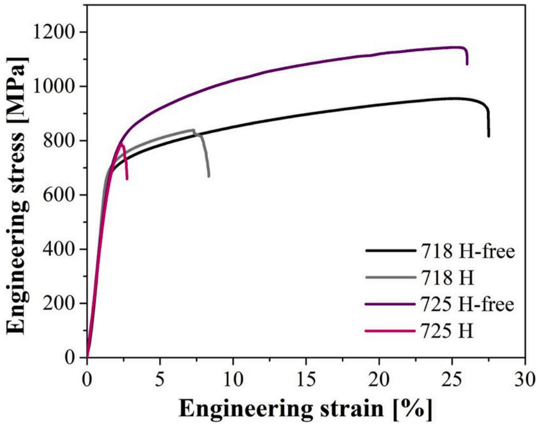

**Fig. 6.** Engineering stress-strain curves of Alloys 718 and 725 tensile tested under hydrogen-free and hydrogen-charged conditions.

### 3.4. Effect of hydrogen on the damage behavior

#### 3.4.1. Fractography

Fig. 8 shows the fractographies of Alloys 718 and 725 after the SSRT until fracture under hydrogen-free and hydrogen-charged conditions. The fracture surface of hydrogen-free Alloy 718 exhibited a microvoid coalescence (MVC)-assisted ductile fracture mode (Fig. 8(a) and (a1)) accompanied by an evident necking. In contrast, the hydrogenated sample exhibited a mixed failure mode, *i.e.* both brittle and ductile failures. In the outer region of the fractured surface, transgranular brittle failure in the form of river patterns, ridges, and steps was observed (Fig. 8(b)). In addition, several flat surfaces indicated intergranular cracking along GBs, as highlighted by the red circles in Fig. 8(b). Nevertheless, most brittle region was dominated by transgranular cracks. In the central region of the fracture surface, the hydrogen-charged sample manifested ductile fracture by the MVC process. A transition from ductile to brittle behavior was observed between the outer and central regions.

For Alloy 725 under hydrogen-free condition, the sample showed a prevalent ductile fracture mode. Besides, intergranular cracks were also present in this sample, as demonstrated by the magnified images in Fig. 8(c1) and (c2). However, such type of cracks was absent in the Alloy 718 sample under hydrogen-free condition. In comparison to hydrogen-charged Alloy 718, a similar fracture feature was observed in the hydrogenated Alloy 725 sample, that is, a mixed failure mode combining both brittle and ductile failures. In particular, the intergranular cracking dominated in the outer brittle region. It is worth noting that the majority of the fractured GB junctions revealed curved morphologies, as marked by the blue ellipses in Fig. 8(d1) and (d2).

#### 3.4.2. Surface and subsurface cracks

To further investigate hydrogen effect on damage behavior, the post-mortem characterization of surface and subsurface cracks was carried out for Alloys 718 and 725 under hydrogen-charged condition, as shown in Figs. 9–11. Consistent with the fractography results (Fig. 8(b)), Alloy 718 primarily fractured by transgranular cracking (Fig. 9(a)). As demonstrated by the inverse pole figure map in Fig. 9(a1), cracking paths followed {111} slip traces (marked in black). In comparison, both primary and secondary cracks in Alloy 725 exhibited intergranular dominant cracking behavior (Fig. 9(b1) and (b2)). The EBSD results implied that the misorientation between adjacent grains along the crack path ranged from 15° to 55°. Additionally, several cracks propagated along twin boundaries and one example is shown in Fig. 9(b1).

On the cross-section near the fracture surface, no noticeable intergranular or transgranular cracks were found in Alloy 718 (Fig. 10(a)). The contrast variation in the matrix (Fig. 10(a)) was caused by plastic

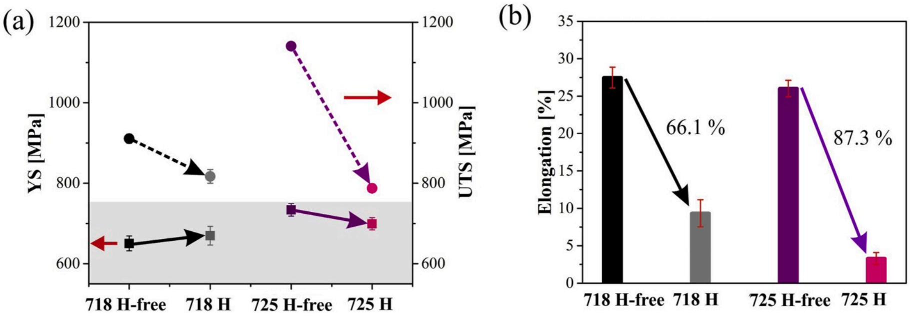

**Fig. 7.** Hydrogen effect on mechanical properties of Alloys 718 and 725: (a) yield strength (YS, change indicated by the solid lines); ultimate tensile strength (UTS, change indicated by the dash lines); and (b) total elongation.

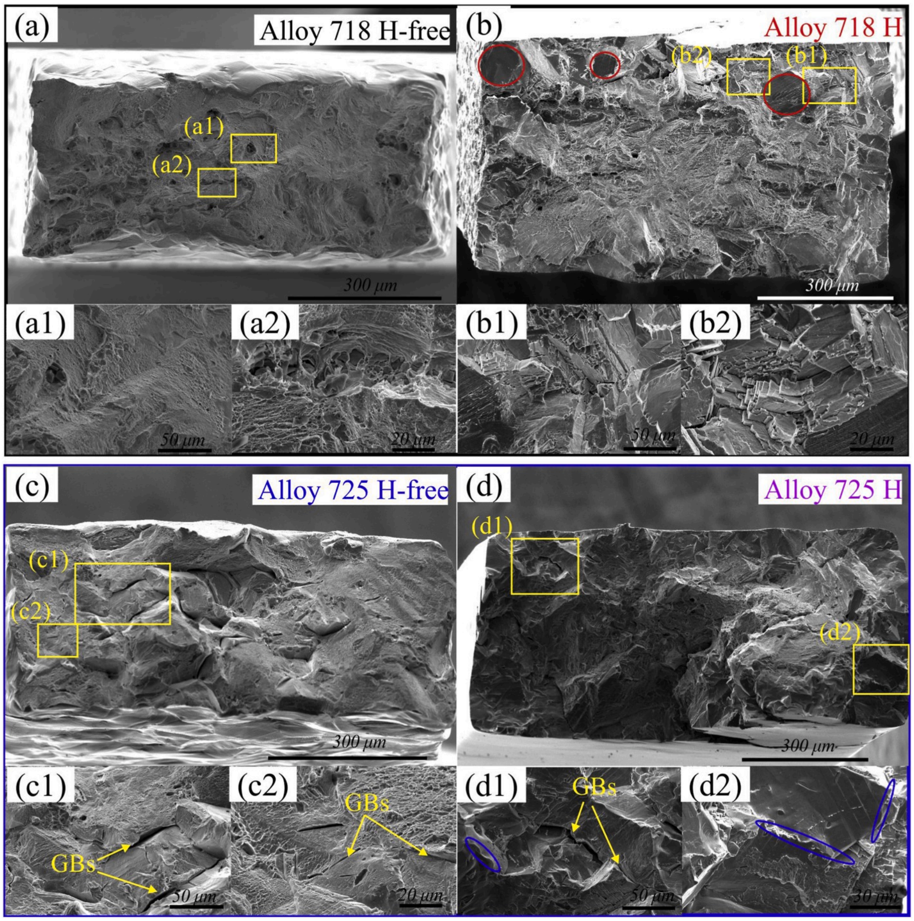

**Fig. 8.** Fractography images of Alloy 718 after loading to fracture in (a)–(a2) hydrogen-free and (b)–(b2) hydrogen-charged conditions; Alloy 725 in (c)–(c2) hydrogen-free and (d)–(d2) hydrogen-charged condition. (GBs: grain boundaries.)

deformation. A large amount of plastic deformation was observed at local high stress concentration regions such as GBs and triple junctions, as well as areas around the small grains. In Alloy 725, several subsurface cracks were observed, as indicated by the yellow boxes in Fig. 10(b). The corresponding EBSD measurements indicated that all these cracks were initiated and propagated along GBs (Fig. 11(a1) and (b1)). Particularly, the curved GBs were more susceptible to cracking (Fig. 11). It can be seen that triple junctions and GBs with complex morphologies readily initiated cracks, as illustrated in red boxes in Fig. 11(a). The high kernel average misorientation values at the cracked GBs and triple junctions involved with small grains indicated localized plasticity in these regions. Such localized deformation could be caused by intensive dislocation interactions.

## 4. Discussion

The results presented in Section 3 showed that Alloys 718 and 725 possessed different microstructures, in terms of grain size, type and size of precipitates. Such microstructural features are deemed to significantly affect the mechanical properties and damage behavior of these two alloys under both hydrogen-free and hydrogen-charged conditions. In this section, we elaborate the correlation between microstructures and the observed mechanical properties as well as the damage behavior. In particular, the role of GB precipitates in embrittlement behavior of both alloys will be discussed.

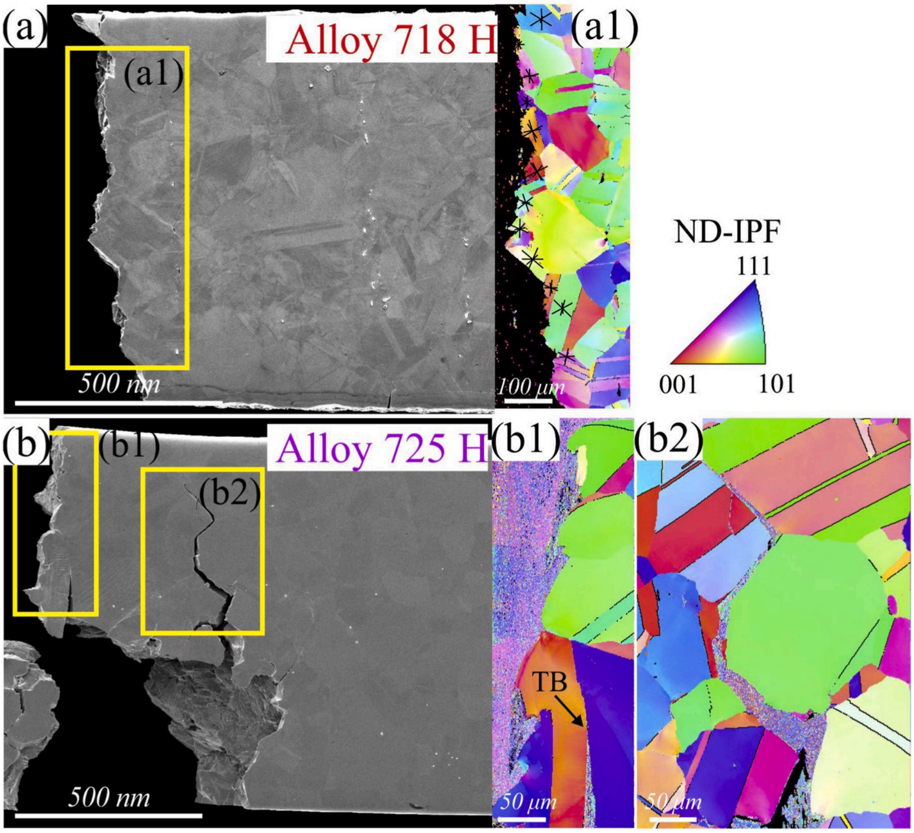

**Fig. 9.** Scanning electron micrographs of surface cracks of (a) Alloy 718 and (b) Alloy 725 after loading to fracture in hydrogen-charged condition and the corresponding inverse pole figures (IPFs) of the selected areas in the yellow frames for (a1) Alloy 718 and (b1)−(b2) Alloy 725. (ND: normal direction; TB: twin boundary.). (For interpretation of the references to colour in this figure legend, the reader is referred to the Web version of this article.)

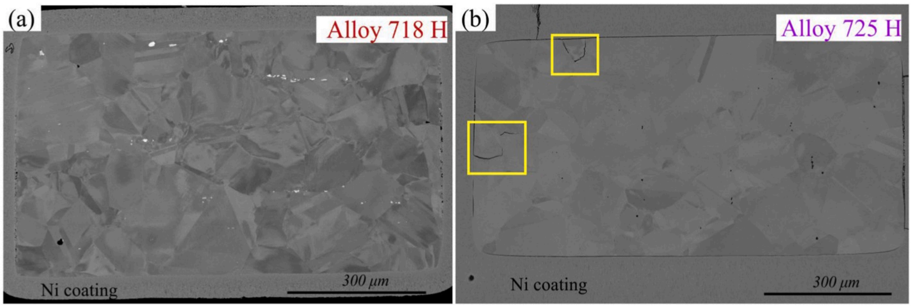

**Fig. 10.** Cross-section microstructures of hydrogen-charged (a) Alloy 718 and (b) Alloy 725 samples after loading to fracture.

### 4.1. *Hydrogen effect on yield strength*

It is worth noting that hydrogen leads to the softening of Alloy 725, as illustrated by the reduction in YS in Fig. 7(a). Such softening effect can be related to the decoration of GBs by (Cr,Mo)-rich precipitates, as shown in Fig. 2(b2) and 4. Compared with Alloy 718, therefore, more hydrogen should be trapped at GBs in Alloy 725 due to the existence of such precipitates. As a result, dislocation nucleation was largely promoted at precipitate-decorated GBs [38,39], and dislocation slip became easier upon loading. In Alloy 718, the presence of hydrogen only resulted in a trivial impact on the yield strength, as demonstrated by a slight increase in yield strength (Fig. 7(a)) even within scatter range. This negligible effect of hydrogen on the yield strength in Alloy 718 should lie in the low population of GB precipitates. With these findings, it is worth emphasizing the important role of GB precipitates (concerning type, number density, and size, *etc.*) in the yield strength in these alloys when hydrogen is present.

### 4.2. *Failure mechanisms under the hydrogen-free condition*

Under hydrogen-free condition, Alloy 718 failed through MVC in a ductile fracture mode. In addition, we observed only a few secondary cracks along the original interfaces between the Nb-enriched δ phases and the matrix (Fig. 12). It needs to be clarified here that some surface δ phase could have been dissolved during electropolishing. Those corrosion-induced geometrical irregularities at the original δ phase and matrix interfaces are local stress concentrators that can initiate cracks readily upon deformation. On the one hand, the adjacent precipitation free zones around the δ precipitates are weak regions that can initiate cracks [40,41], which can be detrimental to the mechanical properties. On the other hand, the needle-like δ precipitates could effectively divert the crack propagation along GBs [42] and such a relief of stress

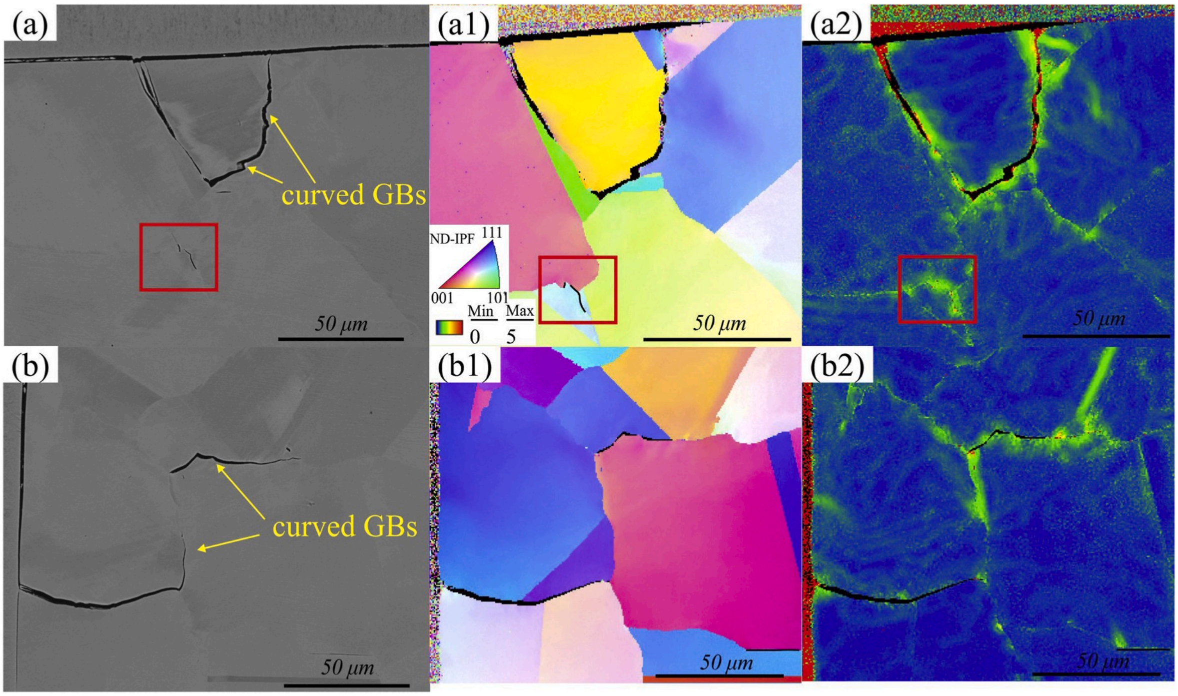

**Fig. 11.** (a) and (b) Backscattered electron micrographs of the cross-section cracks of Alloy 725; (a1) and (b1) corresponding inverse pole figures; (a2) and (b2) corresponding kernel average misorientation maps. (GBs: grain boundaries.)

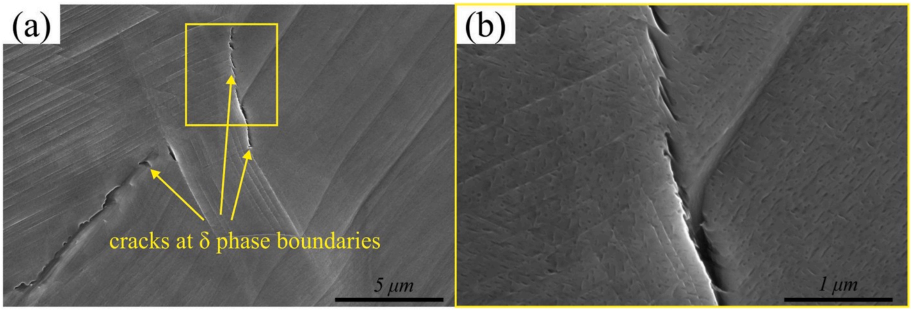

**Fig. 12.** (a) Scanning electron micrograph of secondary cracks along the δ phase boundaries in Alloy 718 after fracture in the hydrogen-free condition and (b) higher magnification of the selected area in (a).

concentration at precipitation free zones would further restrain crack extension [43]. In comparison, carbides and nitrides were generally strong and could be considered to have a slight or no orientation relationship with the matrix [44]. Some of them were cracked during plastic deformation, but those cracks could not extend into the matrix [28]. In contrast to Alloy 718, intergranular cracks were observed on the fractography in Alloy 725, which suggested that GBs are vulnerable sites even without the presence of hydrogen. Such weak GBs can be related to the decoration of incoherent (Cr, Mo)-rich precipitates (Fig. 2(b2)). The effect of those precipitates can be similar to that of the GB carbides [45], which form a dense network at GBs. Those carbides lead to high susceptibility of nickel alloys to intergranular cracking, as voids nucleate readily at those interfaces [45]. Nevertheless, Alloy 725 achieved comparable ductility to Alloy 718 under the hydrogen-free condition. The GB precipitates do not seem to be harmful to ductility in both alloys in the absence of hydrogen.

### *4.3. Failure mechanisms under the hydrogen-charged condition*

#### *4.3.1. Alloy 718*

Under hydrogen-charged condition, transgranular fracture was the prevalent failure mode in Alloy 718. During plastic deformation, the shearing of coherent and ordered γ' and γ'' precipitates lowers the energy required for the trailing dislocations to cut through them on the same slip plane, which leads to the slip planarity [26,46]. The presence of hydrogen can further promote slip planarity by lowering the stacking fault energy (SFE) [8,26]. These facts can result in a high-stress concentration within the slip bands. The local increase in stress concentration and strain discontinuities at the intersections of dislocation slip bands simultaneously attracts hydrogen to these locations. Moreover, hydrogen can promote the formation of defects, *i.e.*, dislocations and vacancies [18,38,47,48]. As a result, the formation and coalescence of microvoids at those local plastic instability sites (intersections of slip bands) are responsible for the primary transgranular cracking [22,27]. Fig. 13 shows an illustration of microvoids generated at dislocation slip bands.

The observed intergranular cracks in Alloy 718 can be attributed to slip localization at GB triple junctions, high misorientation GBs, and δ phase decorated GBs [25,27]. When hydrogen is present, the formation of micro-cracks along the incoherent interfaces between δ precipitate and the matrix becomes easier in the framework of HEDE mechanism [24]. Zhang et al. [28] reported that the GB δ phases are prone to absorb

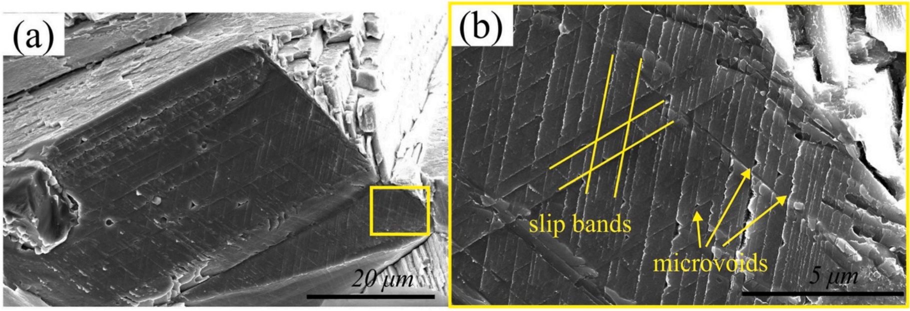

**Fig. 13.** (a) Fractography of Alloy 718 failure after hydrogen charging, and (b) magnified yellow box in (a) showing microvoids initiated at the dislocation slip bands. (For interpretation of the references to colour in this figure legend, the reader is referred to the Web version of this article.)

a large amount of hydrogen than coarse carbides in the matrix during cathodic charging; thus, hydrogen-induced cracking readily initiates along the δ-matrix interfaces, and no cracks can be observed at the interfaces between carbides and the matrix. However, only a limited number of intergranular cracks were observed after fracture in the present study, which could be attributed to a small size and fraction of the δ phase. In comparison, Alloy 718 investigated in Refs. [24,28] exhibited a much higher fraction and larger δ phase along the GBs. At random GBs without the δ phase decoration, a critical amount of hydrogen is required to form intergranular cracks, depending on the nature of the GB and the corresponding stress state [11]. Additionally, GBs with high resistance to dislocation transmission can increase the propensity for intergranular cracking [33].

### *4.3.2. Alloy 725*

For Alloy 725, hydrogen-assisted cracking resulted in an early fracture of the sample shortly after loading to the yield point. From the fractography, a large fraction of intergranular cracking features was observed on the brittle area. A closer observation of the GB crack indicated that the GB was irregularly curved (Fig. 14(b)), those GBs were mostly associated with precipitates, as shown in Fig. 4. The main reason for the irregular shape was the migration of the GB along with the redistribution of alloying elements, and the GB precipitates acted as the sinks during prolonged aging [49]. On one side of the GB, the fractured grain plane was relatively flat, while the plane on the other side exhibited higher roughness with small irregularly shaped humps (Fig. 14(c)). Each hump was linked with a microvoid, as pointed out by the arrows. A previous study demonstrated that, in low alloy 4140 steel, hydrogen atoms were primarily trapped at carbides-matrix interfaces when carbides (size approximately 100 nm) were present along the GBs [50]. And the high susceptibility of that steel to HE was attributed to the debonding at GB carbides [50]. The similar cracking behavior in this study indicated that GB precipitates promoted the formation of microvoids at the interfaces during plastic deformation and had a detrimental effect on the mechanical properties of Alloy 725.

Recently, Turk et al. [51] studied the effect of GB precipitates on the hydrogen diffusion in an Fe–Ni alloy by performing thermal desorption tests and GB diffusion modeling. They proposed that GB precipitates effectively hinder hydrogen diffusion along the GBs and cause a decrease in hydrogen absorption. This is an unusual phenomenon because the trapped hydrogen content should increase with an increasing number of precipitates [4,52]. The postulated reason for this unconventional phenomenon is the alteration of local hydrogen diffusivity by the presence of a dense network of GB precipitates [51]. In this study, GB precipitates seem to have a slight effect on the hydrogen absorption ability of this alloy. The inconsistent results between the current study and Ref. [51] could be due to several reasons, such as the differences in grain size, hydrogen charging condition, fraction, distribution, composition of the GB precipitates, *etc*. Compared with Ref. [51], the fewer dense precipitates along the GBs and the halved grain size in Alloy 725 in the current study could guarantee that the GBs are still fast-diffusion pathways for hydrogen, and thus enabling intergranular cracking when a certain amount of hydrogen is trapped by the GB precipitates.

The TDA results indicated that the hydrogen absorption ability for the two studied alloys was not identical. The diffusible hydrogen is generally considered as the main reason for HE [53]. However, the interactions between dislocations and hydrogen-decorated precipitates are deemed to be the major reason for the distinct brittle phenomenon in the current study. The reason for this postulation was that Alloy 718 absorbed a comparable amount of diffusible hydrogen as Alloy 725 (~29%), but the former was more resistant to HE (Table 2). Albeit, Alloy 725 trapped more reversible hydrogen (56.8%) than Alloy 718 (50.9%). The known reversible trapping sites for hydrogen are γ', γ'', δ phases, GBs, and edge dislocations [35,36,54,55]. Note that those GBs refer to the precipitate-free state. The amount of hydrogen trapped by the coherent γ' and γ'' precipitates is highly dependent on the size of the interfacial area, and the size of precipitates affects the trapping activation energy [56]. Specifically, as the sizes of γ' and γ'' increases, their coherency with the matrix decreases. As a result, the change in the elastic-stress field around the precipitates increases the trapping activation energy, and hydrogen trapping becomes more reluctant. Considering the size of the precipitates in the two alloys, γ'' phase in Alloy 725 had a larger interfacial area per unit volume and higher coherency with the matrix. Thus, Alloy 725 contained more reversibly trapped hydrogen. In addition, the complex features of the precipitate-decorated GBs should also be considered. Until now, no

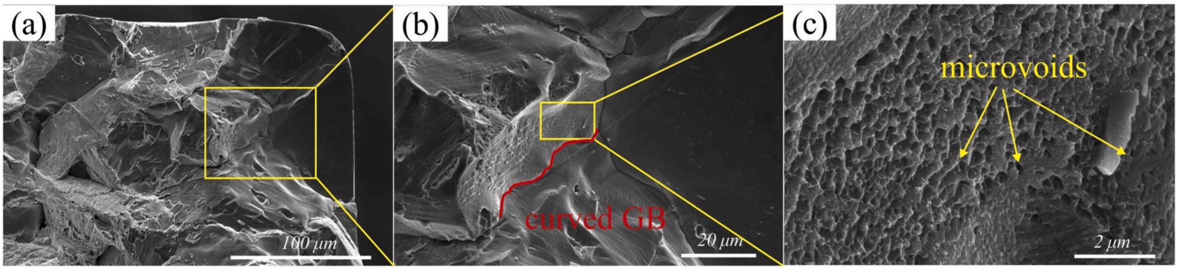

**Fig. 14.** (a) Fractography of Alloy 725 failure after hydrogen charging showing (b) curved GB and (c) microvoids on the fractured GB surface.

quantitative results have been provided in the literature on the effect of GB precipitates (here (Cr, Mo)-rich precipitates) on the GB trapping energy. Precipitate-free GBs are referred to as reversible traps, however, the trapping behavior of GBs with precipitates might become less reversible depending on the structure and chemistry of the precipitates as well as their special crystallographic arrangement with the matrix. Those precipitates could be the sinks or sources for hydrogen exchange [57], which highly determine the susceptibility of Alloy 725 to HE. The nano-sized precipitate could lead to local distortion of the lattice at GBs. Upon deformation, dislocations pile up at those GBs. The dislocations either are difficult to transmit through GBs or can be absorbed by GBs due to the disordered GB structures. As a result, local stress concentration increases, which causes the formation of micro-cracks and debonding of GBs, as observed in Alloy 725 under hydrogen-free condition. This phenomenon becomes more pronounced when hydrogen is present because trapped hydrogen lowers the defect-formation energy and promotes the formation of vacancies. When plastic deformation occurs, those interfaces become stress concentrators that attract hydrogen and further promote vacancy formation and crack initiation.

The present study revealed that Alloy 725 possesses more attractive mechanical properties (in terms of YS and UTS) than Alloy 718 under the hydrogen-free condition, though, (Cr, Mo)-rich GB precipitate in Alloy 725 is detrimental to its resistance to HE. The systematic investigation of the local deformation behavior at precipitate-decorated GBs is required in further study to understand the effect of hydrogen on the local deformation mechanisms, possibly by employing in-situ small-scale tests together with advanced microstructural characterization techniques, such as focused ion beam milling and transmission electron microscopy. To manipulate (Cr, Mo)-rich GB precipitate (concerning its chemistry, size, and fraction, *etc.*) by adjusting heat treatments could be an effective measure to mitigate the severe HE in such alloy, making it more suitable for oil and gas industry applications in the framework of GB engineering.

## 5. Conclusions

In this study, hydrogen embrittlement behavior of Alloys 718 and 725 was investigated using the slow strain-rate tensile test combined with advanced characterization techniques, *i.e.*, scanning electron microscopy, electron backscatter diffraction, thermal desorption analysis, and atom probe tomography, *etc*. The susceptibility of these two alloys to hydrogen embrittlement was discussed in relation to their respective microstructures. The main conclusions are summarized as follows.

1) Compared with a small volume fraction of δ phase at grain boundaries in Alloy 718, a large volume fraction of grain boundaries in Alloy 725 was decorated with (Cr, Mo)-rich precipitates. Such differences in the type and fraction of grain-boundary precipitates in these alloys resulted in different yielding and damage behavior in both hydrogen-free and hydrogen-charged conditions.
2) In the hydrogen-free condition, Alloy 725 exhibited a higher yield strength and ultimate tensile strength than Alloy 718 in a similar ductility level. Alloy 718 failed through microvoid coalescence ductile fracture mode, while Alloy 725 failed through a combination of transgranular microvoid coalescence and intergranular cracking. Such intergranular cracking was considered to relate to the grain boundary (Cr, Mo)-rich precipitates in Alloy 725.
3) In the hydrogen-charged condition, Alloy 725 exhibited a lower resistance to hydrogen embrittlement than Alloy 718. A mixture of transgranular and intergranular cracking feature was observed on the fracture surface of Alloy 718, while intergranular fracture dominated in Alloy 725.
4) The (Cr, Mo)-rich precipitates in Alloy 725 changed the morphology of grain boundaries and resulted in more locally disordered lattice structures. Such grain boundaries have a higher propensity for cracking when the local stress concentration reaches the critical value for crack initiation during plastic deformation. With the presence of hydrogen, the formation of microvoids becomes easier. As a result, intergranular cracking occurs readily and results in a low ductility of the alloy.

## Declaration of competing interest

The authors declare that they have no known competing financial interests or personal relationships that could have appeared to influence the work reported in this paper.

## CRediT authorship contribution statement

**Xu Lu:** Conceptualization, Methodology, Investigation, Data curation, Writing - original draft. **Yan Ma:** Investigation, Data curation, Writing - review & editing. **Dong Wang:** Data curation, Investigation, Writing - review & editing.

## Acknowledgements

X. Lu acknowledges the financial support from the COMET program within the K2 Center “Integrated Computational Material, Process and Product Engineering (IC-MPPE)” (Project No 859480). This program was supported by the Austrian Federal Ministries for Climate Action, Environment, Energy, Mobility, Innovation and Technology (BMK) and for Digital and Economic Affairs (BMDW), represented by the Austrian research funding association (FFG), and the federal states of Styria, Upper Austria and Tyrol. D. Wang acknowledges the financial support from the Research Council of Norway through the project HyLINE (294739). Voestalpine Böhler Edelstahl GmbH & Co KG is acknowledged for providing laboratory-scale Alloy 725 samples and Aker Solutions for Alloy 718 samples.

## Appendix A. Supplementary data

Supplementary data to this article can be found online at https://doi.org/10.1016/j.msea.2020.139785.

## References

[1] R.B. Bhavsar, A. Collins, S. Silverman, Use of alloy 718 and 725 in oil and gas industry, Superalloys 718 (2001) 47–55, 625, 706 and Various Derivatives.
[2] M. Iannuzzi, A. Barnoush, R. Johnsen, Materials and corrosion trends in offshore and subsea oil and gas production, npj Mater. Degrad. 1 (1) (2017) 2.
[3] H.S. Klapper, J. Klower, O. Gosheva, Hydrogen embrittlement: the game changing factor in the applicability of nickel alloys in oilfield technology, Philos. Trans. R. Soc. A 375 (2098) (2017).
[4] L.F. Liu, K. Tanaka, A. Hirose, K.F. Kobayashi, Effects of precipitation phases on the hydrogen embrittlement sensitivity of Inconel 718, Sci. Technol. Adv. Mater. 3 (4) (2002) 335–344.
[5] R. Krakow, D.N. Johnstone, A.S. Eggeman, D. Hunert, M.C. Hardy, C.M.F. Rae, P. A. Midgley, On the crystallography and composition of topologically close-packed phases in ATI 718Plus (R), Acta Mater. 130 (2017) 271–280.
[6] N. Totsuka, E. Lunarska, G. Cragnolino, Z. Szklarskasmialowska, Effect of hydrogen on the intergranular stress-corrosion cracking of Alloy-600 in high-temperature aqueous environments, Corrosion 43 (8) (1987) 505–514.
[7] Y. Yao, X.L. Pang, K.W. Gao, Investigation on hydrogen induced cracking behaviors of Ni-base alloy, Int. J. Hydrogen Energy 36 (9) (2011) 5729–5738.
[8] P.D. Hicks, C.J. Altstetter, Internal hydrogen effects on tensile properties of iron-base and nickel-base superalloys, Metall. Mater. Trans. 21 (2) (1990) 365–372.
[9] A.M. Brass, J. Chene, Influence of deformation on the hydrogen behavior in iron and nickel base alloys: a review of experimental data, Mater. Sci. Eng. 242 (1-2) (1998) 210–221.
[10] J. Chene, A.M. Brass, Role of temperature and strain rate on the hydrogen-induced intergranular rupture in alloy 600, Metall. Mater. Trans. 35a (2) (2004) 457–464.
[11] A. Kimura, H.K. Birnbaum, Hydrogen induced grain-boundary fracture in high-purity nickel and its alloys - enhanced hydrogen diffusion along grain-boundaries, Acta Metall. 36 (3) (1988) 757–766.
[12] H.K. Birnbaum, P. Sofronis, Hydrogen-enhanced localized plasticity - a mechanism for hydrogen-related fracture, Mater. Sci. Eng. 176 (1-2) (1994) 191–202.
[13] H.K. Birnbaum, Mechanisms of Hydrogen Related Fracture of Metals, Illinois University at Urbana department of materials science and engineering, 1989.
[14] L.B. Pfeil, The effect of occluded hydrogen on the tensile strength of iron, Proc. Roy. Soc. Lond. 112 (1926) 182–195.

[15] W.W. Gerberich, Modeling hydrogen induced damage mechanisms in metals, in: Gaseous Hydrogen Embrittlement of Materials in Energy Technologies, vol. 2, 2012, pp. 209–246.

[16] C.J. McMahon, Hydrogen-induced intergranular fracture of steels, Eng. Fract. Mech. 68 (6) (2001) 773–788.

[17] S.P. Lynch, Environmentally assisted cracking - overview of evidence for an adsorption-induced localized-slip process, Acta Metall. 36 (10) (1988) 2639–2661.

[18] S. Lynch, Hydrogen embrittlement phenomena and mechanisms, Corrosion Rev. 30 (3-4) (2012) 105–123.

[19] S.P. Lynch, Metallographic contributions to understanding mechanisms of environmentally assisted cracking, Metallography 23 (2) (1989) 147–171.

[20] S.P. Lynch, Mechanisms of hydrogen-assisted cracking, Met. Forum 2 (3) (1979) 189–200.

[21] M. Nagumo, Hydrogen related failure of steels - a new aspect, Mater. Sci. Technol. 20 (8) (2004) 940–950.

[22] Z. Zhang, G. Obasi, R. Morana, M. Preuss, Hydrogen assisted crack initiation and propagation in a nickel-based superalloy, Acta Mater. 113 (2016) 272–283.

[23] I.M. Robertson, H.K. Birnbaum, An hvem study of hydrogen effects on the deformation and fracture of nickel, Acta Metall. 34 (3) (1986) 353–366.

[24] Z. Tarzimoghadam, D. Ponge, J. Klower, D. Raabe, Hydrogen-assisted failure in Ni-based superalloy 718 studied under in situ hydrogen charging: the role of localized deformation in crack propagation, Acta Mater. 128 (2017) 365–374.

[25] S. Jothi, S.V. Merzlikin, T.N. Croft, J. Andersson, S.G.R. Brown, An investigation of micro-mechanisms in hydrogen induced cracking in nickel-based superalloy 718, J. Alloys Compd. 664 (2016) 664–681.

[26] L. Xiao, D.L. Chen, M.C. Chaturvedi, Shearing of γ″ precipitates and formation of planar slip bands in Inconel 718 during cyclic deformation, Scripta Mater. 52 (7) (2005) 603–607.

[27] V. Demetriou, J.D. Robson, M. Preuss, R. Morana, Study of the effect of hydrogen charging on the tensile properties and microstructure of four variant heat treatments of nickel alloy 718, Int. J. Hydrogen Energy 42 (37) (2017) 23856–23870.

[28] Z.B. Zhang, K.L. Moore, G. McMahon, R. Morana, M. Preuss, On the role of precipitates in hydrogen trapping and hydrogen embrittlement of a nickel-based superalloy, Corrosion Sci. 146 (2019) 58–69.

[29] M. Seita, J.P. Hanson, S. Gradecak, M.J. Demkowicz, The dual role of coherent twin boundaries in hydrogen embrittlement, Nat. Commun. 6 (2015).

[30] J.P. Hanson, A. Bagri, J. Lind, P. Kenesei, R.M. Suter, S. Gradecak, M. J. Demkowicz, Crystallographic character of grain boundaries resistant to hydrogen-assisted fracture in Ni-base alloy 725, Nat. Commun. 9 (2018).

[31] R. Kirchheim, Hydrogen solubility and diffusivity in defective and amorphous metals, Prog. Mater. Sci. 32 (4) (1988) 261–325.

[32] D. Wang, X. Lu, Y. Deng, X. Guo, A. Barnoush, Effect of hydrogen on nanomechanical properties in Fe-22Mn-0.6C TWIP steel revealed by in-situ electrochemical nanoindentation, Acta Mater. 166 (2019) 618–629.

[33] X. Lu, D. Wang, D. Wan, Z.B. Zhang, N. Kheradmand, A. Barnoush, Effect of electrochemical charging on the hydrogen embrittlement susceptibility of alloy 718, Acta Mater. 179 (2019) 36–48.

[34] X. Lu, Hydrogen Assited Cracking in Alloy 725 Revisited, Manuscript in Preparation, 2020.

[35] A. Turnbull, R.G. Ballinger, I.S. Hwang, M.M. Morra, M. Psailadombrowski, R. M. Gates, Hydrogen transport in nickel-base alloys, Metall. Mater. Trans. 23 (12) (1992) 3231–3244.

[36] L. Liu, C. Zhai, C. Lu, W. Ding, A. Hirose, K.F. Kobayashi, Study of the effect of δ phase on hydrogen embrittlement of Inconel 718 by notch tensile tests, Corrosion Sci. 47 (2) (2005) 355–367.

[37] Standard Practice for Slow Strain Rate Testing to Evaluate the Susceptibility of Metallic Materials to Environmentally Assisted Cracking, 2013.

[38] R. Kirchheim, Reducing grain boundary, dislocation line and vacancy formation energies by solute segregation. I. Theoretical background, Acta Mater. 55 (15) (2007) 5129–5138.

[39] R. Kirchheim, Reducing grain boundary, dislocation line and vacancy formation energies by solute segregation II. Experimental evidence and consequences, Acta Mater. 55 (15) (2007) 5139–5148.

[40] V. Demetriou, J.D. Robson, M. Preuss, R. Morana, Effect of hydrogen on the mechanical properties of alloy 945X (UNS N09945) and influence of microstructural features, Mater. Sci. Eng. 684 (2017) 423–434.

[41] L.A. James, W.J. Mills, Effect of heat-treatment and heat-to-heat variations in the fatigue-crack growth-response of alloy 718, Eng. Fract. Mech. 22 (5) (1985) 797–817.

[42] G.I. Sjoberg, N.G. Flygrnotor, Grain Boundary δ-phase Morphologies, Carbides and Notch Rupture Sensitivity of Cast Alloy 718 Superalloys 718, 625, 706 and Various Derivatives, 1991, pp. 603–620.

[43] C.Z. Wang, R.B. Li, Effect of double aging treatment on structure in Inconel 718 alloy, J. Mater. Sci. 39 (7) (2004) 2593–2595.

[44] H. Kitaguchi, Metallurgy – Advances in Materials and Processes, InTech, 2012.

[45] S. Lynch, A review of underlying reasons for intergranular cracking for a variety of failure modes and materials and examples of case histories, Eng. Fail. Anal. 100 (2019) 329–350.

[46] M. Sundararaman, P. Mukhopadhyay, S. Banerjee, Deformation-behavior of gamma`` strengthened inconel-718, Acta Metall. 36 (4) (1988) 847–864.

[47] M. Nagumo, K. Takai, The predominant role of strain-induced vacancies in hydrogen embrittlement of steels: Overview, Acta Mater. 165 (2019) 722–733.

[48] A. Pundt, R. Kirchheim, Hydrogen in metals: microstructural aspects, Annu. Rev. Mater. Res. 36 (2006) 555–608.

[49] D.N. Yoon, M.F. Henry, M. Jackson, Precipitation induced grain boundary migration in austenitic alloys, J. Phys. Colloq. 51 (C1) (1990) 721–726.

[50] Y.F. Jiang, B. Zhang, Y. Zhou, J.Q. Wang, E.H. Han, W. Ke, Atom probe tomographic observation of hydrogen trapping at carbides/ferrite interfaces for a high strength steel, J. Mater. Sci. Technol. 34 (8) (2018) 1344–1348.

[51] A. Turk, D. Bombac, J.J. Rydel, M. Zietara, P.E.J. Rivera-Diaz-del-Castillo, E. I. Galindo-Nava, Grain boundary carbides as hydrogen diffusion barrier in a Fe-Ni alloy: a thermal desorption and modelling study, Mater. Des. 160 (2018) 985–998.

[52] G.A. Young, J.R. Scully, Evidence that carbide precipitation produces hydrogen traps in Ni-17Cr-8Fe alloys, Scripta Mater. 36 (6) (1997) 713–719.

[53] N. Bailey, Hydrogen Cracking, Woodhead Publishing, 1994.

[54] A. Oudriss, J. Creus, J. Bouhattate, E. Conforto, C. Berziou, C. Savall, X. Feaugas, Grain size and grain-boundary effects on diffusion and trapping of hydrogen in pure nickel, Acta Mater. 60 (19) (2012) 6814–6828.

[55] Q.Q. Cui, J.S. Wu, D.H. Xie, X.G. Wu, Y.H. Huang, X.G. Li, Effect of nanosized NbC precipitates on hydrogen diffusion in X80 pipeline steel, Materials 10 (7) (2017).

[56] F.G. Wei, K. Tsuzaki, Quantitative analysis on hydrogen trapping of TiC particles in steel, Metall. Mater. Trans. 37a (2) (2006) 331–353.

[57] G.M. Pressouyre, Trap theory of hydrogen embrittlement, Acta Metall. 28 (7) (1980) 895–911.